J. Fluid Mech. (2011), *vol.* 679, *pp.* 263–287.
doi:10.1017/jfm.2011.136

Direct numerical simulation of the flow over a sphere at $Re = 3700$

IVETTE RODRIGUEZ[1], RICARD BORELL[2], ORIOL LEHMKUHL[1,2], CARLOS D. PEREZ SEGARRA[1] and ASSENSI OLIVA[1]†

[1]Centre Tecnològic de Transferència de Calor (CTTC), Universitat Politècnica de Catalunya (UPC), 08222 Spain

[2]Termo Fluids S.L., 08222 Spain

(Received 6 May 2010; revised 1 February 2011; accepted 15 March 2011; first published online 19 May 2011)

The direct numerical simulation of the flow over a sphere is performed. The computations are carried out in the sub-critical regime at $Re = 3700$ (based on the free-stream velocity and the sphere diameter). A parallel unstructured symmetry-preserving formulation is used for simulating the flow. At this Reynolds number, flow separates laminarly near the equator of the sphere and transition to turbulence occurs in the separated shear layer. The vortices formed are shed at a large-scale frequency, $S_t = 0.215$, and at random azimuthal locations in the shear layer, giving a helical-like appearance to the wake. The main features of the flow including the power spectra of a set of selected monitoring probes at different positions in the wake of the sphere are described and discussed in detail. In addition, a large number of turbulence statistics are computed and compared with previous experimental and numerical data at comparable Reynolds numbers. Particular attention is devoted to assessing the prediction of the mean flow parameters, such as wall-pressure distribution, skin friction, drag coefficient, among others, in order to provide reliable data for testing and developing statistical turbulence models. In addition to the presented results, the capability of the methodology used on unstructured grids for accurately solving flows in complex geometries is also pointed out.

Key words: turbulence simulation, vortex shedding, wakes

1. Introduction

The unsteady flow over a sphere at sub-critical Reynolds numbers has a complex nature characterized by the transition from laminar to turbulent flow, the existence of a turbulent wake and the unsteady shedding of vortices in the wake. This flow has been an object of many experimental (Achenbach 1972, 1974; Kim & Durbin 1988; Sakamoto & Haniu 1990; Jang & Lee 2007) and numerical (Seidl, Muzaferija & Peric 1998; Tomboulides & Orszag 2000; Ploumhans *et al.* 2002; Constantinescu & Squires 2003) studies. In these works, the wake configuration and the shedding mechanism were investigated at different Reynolds numbers. They have also provided distribution of the pressure coefficient and skin friction over the sphere, and integral parameters such as the dominant shedding frequencies and the drag coefficient, among others.

† Email address for correspondence: cttc@cttc.upc.edu

In the sub-critical range, $800 \leqslant Re \leqslant 3.7 \times 10^5$ (i.e. the shear layer is laminar at separation from the sphere but the wake is turbulent), most of the experimental works have been focused on the observations of the shedding mechanisms and instabilities in the shear layer. In the works of Achenbach (1972, 1974), the vortex shedding from spheres in the range of $400 < Re < 5 \times 10^6$ was investigated experimentally. He found the co-existence of two Strouhal numbers and suggested that the vortex separation occurs at a point that rotates around the sphere with the vortex-shedding frequency. Later, Taneda (1978) made flow visualizations in the range of $Re = 10^4$–10^6. It was suggested that in the sub-critical range, wave motion occurs in a plane that contains the streamwise axis and rotates slowly and randomly around it. Kim & Durbin (1988) carried out experiments in the wake of the sphere for Reynolds numbers in the range of $500 \leqslant Re \leqslant 6 \times 10^4$. They observed two frequency modes of instabilities: (i) a low-frequency mode related to the large-scale instability of the wake and (ii) a high-frequency mode associated with the small-scale instabilities of the separating shear layer. In addition, they also provided measurements of the streamwise velocity at different distances from the sphere for a flow with and without acoustic excitation at $Re = 3700$. Their results showed that the flow excited shortens the length of the recirculation bubble. Sakamoto & Haniu (1990) investigated experimentally the vortex shedding from spheres in the range of $300 \leqslant Re \leqslant 4 \times 10^4$. They classified the vortex-shedding pattern as a function of the Reynolds number, and they also measured the low- and high-frequency modes of unsteadiness. Recently, Jang & Lee (2007) carried out visualizations of the turbulent flow at $Re = 5300$ and $Re = 11\,000$ providing some measurements of the turbulent Reynolds stresses and the turbulent kinetic energy in the wake of the sphere for $Re = 11\,000$.

Regarding numerical techniques, several simulations of the flow in the sub-critical regime have been carried out. These computations have also contributed to a better understanding of the fluid dynamics and vortex-shedding mechanisms. In order to study the transitions in the wake as a function of the Reynolds number, Tomboulides, Orszag & Karniadakis (1993) and Tomboulides & Orszag (2000) performed large eddy simulations (LES) for $Re = 20\,000$ and time-accurate direct numerical simulations (DNS) up to $Re = 1000$, respectively. They also reported some instantaneous and mean flow data statistics being in good agreement with previous experimental results. Seidl *et al.* (1998) carried out experimental and DNS studies of the flow behind a sphere held by a cylindrical stick at $Re = 5000$. Although the reported information is not exhaustive, the results provided can be useful for model comparisons.

More recently, Constantinescu & Squires (2003) carried out LES and detached-eddy simulation (DES) for investigating the flow behind a sphere at $Re = 10^4$. They performed these calculations using an O-type mesh revolved in the azimuthal direction and found that both approaches successfully reproduced the main flow features associated with the vortex shedding. After this study, they also performed DES for the sub-critical and supercritical regimes at Reynolds numbers in the range of 10^4–10^6, capturing with quite good agreement the main flow parameters (see Constantinescu & Squires 2004). Bakic, Schmid & Stankovic (2006) carried out experiments and LES of the flow around a sphere at $Re = 5 \times 10^4$ with reasonable agreement between numerics and experiments. Yun, Kim & Choi (2006) used an immersed boundary method for studying the shear layer and wake instabilities at $Re = 3.7 \times 10^3$ and $Re = 10^4$ by means of LES modelling. They discretized the equations in a body-fitted O–O-type mesh rotated in the azimuthal direction. Their results for the streamwise velocity profile in the wake are in reasonably good agreement with the experimental

data of Kim & Durbin (1988), but a certain uncertainty was found at a distance of three diameters from the sphere.

Although several research works have been carried out up to now, quantitative measurements of the wake characteristics are scarce and there is a lack of a complete set of detailed experimental or numerical data such as detachment angle, recirculation length and first- and second-order turbulence statistics in the wake of the sphere. These data would not only be important for a better understanding of the flow dynamics but also for the development and validation of new turbulence models. However, obtaining reliable experimental results imply several difficulties such as finding an adequate supporting mechanism for the sphere and also accurate measurement techniques along the sphere surface and in the near wake.

On the other hand, in the last few decades DNS has become a powerful tool for providing time-accurate instantaneous and statistical flow data. However, the three-dimensional (3-D) and time-depending flow behaviour demand the use of fine grids and large integration times, which require a large amount of time and computational resources. For this reason, the detailed information about turbulent statistics in the wake of the sphere has been limited up to relatively low Reynolds numbers, most of them in the laminar regime (Mittal & Najjar 1999; Tomboulides & Orszag 2000; Ploumhans *et al.* 2002). To mitigate in some degree the computational requirements of DNS, the modellization of some of the turbulence scales (e.g. LES modelling) is a common alternative. In addition, the evolution of parallel computers, which can be commonly formed by thousands of CPUs, also allows us to multiply the size of the discretizations and the time-integration period. Therefore, in order to solve increasingly complex problems, modelling the turbulence and developing algorithms which can be more efficient on the parallel architectures available are both valuable strategies.

Considering the state of the art, the aim of this work is to study the vortex-shedding dynamics and wake characteristics of the flow behind a sphere at a Reynolds number $Re = 3700$, as well as to provide detailed information about the first- and second-order turbulent statistics of the flow by means of DNS. As far as the author's knowledge is concerned, these are the first DNS results of the flow past a sphere at this Reynolds number. The computations have been performed using a parallel unstructured symmetry-preserving formulation for accurately solving flows in complex geometries. The Poisson equation, which arises from the incompressibility constraint, has been solved by means of a Fourier diagonalization method which takes advantage of the homogeneity of the discretization used in the azimuthal direction. Numerical details about the formulation used and the parallel algorithm are given in the following sections. Results from the computations are presented in terms of instantaneous and statistical data. Moreover, the capability of the presented numerical methodology for performing DNS on unstructured grids with reliable results is also pointed out.

2. Mathematical and numerical model

The Navier–Stokes and continuity equations can be written as

$$M\boldsymbol{u} = \boldsymbol{0} \tag{2.1}$$

$$\frac{\partial \boldsymbol{u}}{\partial t} + C(\boldsymbol{u})\,\boldsymbol{u} + \nu D\boldsymbol{u} + \rho^{-1} G\boldsymbol{p} = \boldsymbol{0}, \tag{2.2}$$

where $\boldsymbol{u} \in \mathbb{R}^{3m}$ and $\boldsymbol{p} \in \mathbb{R}^{m}$ are the velocity vector and pressure, respectively (here m refers to the total number of control volumes (CVs) of the discretized domain), ν is

the kinematic viscosity and ρ is the density. Convective and diffusive operators in the momentum equation for the velocity field are given by $C(\boldsymbol{u}) = (\boldsymbol{u} \cdot \nabla) \in \mathbb{R}^{3m \times 3m}$ and $D = -\nabla^2 \in \mathbb{R}^{3m \times 3m}$ respectively. The gradient and divergence (of a vector) operators are given by $G = \nabla \in \mathbb{R}^{3m \times m}$ and $M = \nabla \cdot \in \mathbb{R}^{m \times 3m}$ respectively.

The governing equations have been discretized on a collocated unstructured grid arrangement by means of second-order spectro-consistent schemes (see Verstappen & Veldman 2003). Such schemes are conservative, i.e. they preserve the kinetic energy equation. These conservation properties are held if and only if the discrete convective operator is skew-symmetric ($C_c(\boldsymbol{u}_c) = -C_c^*(\boldsymbol{u})$), the negative conjugate transpose of the discrete gradient operator is exactly equal to the divergence operator ($-(\Omega_c G_c)^* = M_c$) and the diffusive operator D_c is symmetric and positive-definite (the sub-index c holds for the cell-centred discretization). These properties ensure both stability and conservation of the kinetic-energy balance even at high Reynolds numbers and with coarse grids.

For the temporal discretization of the momentum equation (2.2), a fully explicit second-order Adams–Bashforth scheme has been used for the convective and diffusive terms, while for the pressure gradient term, an implicit first-order scheme has been used.

The velocity–pressure coupling has been solved by means of a classical fractional step projection method,

$$\boldsymbol{u}_c^p = \boldsymbol{u}_c^{n+1} + G\tilde{\boldsymbol{p}}_c, \tag{2.3}$$

where $\tilde{\boldsymbol{p}}_c = \boldsymbol{p}_c^{n+1}\Delta t^n/\rho$ is the pseudo-pressure, $\boldsymbol{u}_c^p$ is the predicted velocity, $n+1$ is the instant when the temporal variables are calculated, and Δt^n is the current time step ($\Delta t^n = t^{n+1} - t^n$). Taking the divergence of (2.3) and applying the incompressibility condition yields a discrete Poisson equation for $\tilde{\boldsymbol{p}}_c$: $L_c\tilde{\boldsymbol{p}}_c = M_c\boldsymbol{u}_c^p$. The discrete Laplacian operator $L_c \in \mathbb{R}^{m \times m}$ is, by construction, a symmetric positive definite matrix ($L_c \equiv M\Omega^{-1}M^*$). Once the solution of $\boldsymbol{p}_c^{n+1}$ is obtained, $\tilde{\boldsymbol{p}}_c$ results from (2.3).

Finally the mass-conserving velocity at the faces ($M_s\boldsymbol{u}_s^{n+1} = 0$) is obtained from the correction:

$$\boldsymbol{u}_s^{n+1} = \boldsymbol{u}_s^p - G_s\tilde{\boldsymbol{p}}_c, \tag{2.4}$$

where G_s represents the discrete gradient operator at the CV faces. This approximation allows us to conserve the mass at the faces but it has several implications. If the conservative term is computed using $\boldsymbol{u}_s^{n+1}$, in practice an additional term proportional to the third-order derivative of $\boldsymbol{p}_c^{n+1}$ is introduced. Thus, in many aspects, this approach is similar to the popular Rhie & Chow (1983) interpolation method and eliminates checkerboard modes.

However, collocated meshes do not conserve the kinetic energy, as has been shown by Morinishi *et al.* (1998) for finite-difference schemes and by Felten & Lund (2006) for finite-volume schemes. When the fractional step method on a collocated arrangement is used, there are two sources of errors in the kinetic energy conservation: (i) due to interpolation schemes and (ii) due to inconsistency in the pressure field in order to ensure mass conservation. While the first one can be eliminated through the use of conservative schemes such as those used in the present work, the latter equals

$$\epsilon_{ke} = (\tilde{\boldsymbol{p}}_c)^* M_c(G_c - G_s)\tilde{\boldsymbol{p}}_c. \tag{2.5}$$

This contribution of the pressure gradient term to the evolution of the kinetic energy cannot be eliminated. Felten & Lund (2006) have conducted a study to determine its scaling order. They have shown that the spatial term of the pressure error scales as $O(\Delta x^2)$ and the temporal term scales as $O(\Delta t)$, i.e. pressure errors are of the order

of $O(\Delta x^2\,\Delta t)$. However, in their work they have proved that pressure errors do not have a significant impact on the results at grid resolutions and time steps used in LES and DNS.

3. Computational aspects: solving the Poisson equation

In the parallel code used to perform the simulations presented in this paper, the algorithm followed at each time step can be divided into two parts: (i) an implicit part where the Poisson equation is solved to project the velocity field into a divergence-free space (this is usually the main bottleneck from the computational point of view) and (ii) the rest of the calculations which are carried out in an explicit manner.

The mesh used for solving the domain is generated by a constant step rotation of a two-dimensional (2-D) unstructured grid about the axis (extrusion), $2\pi/N_{planes}$ being the step size (N_{planes} is the number of planes in which the azimuthal direction is divided). Under these conditions, the azimuthal coupling of the discrete Poisson equation results into circulant sub-matrices that are diagonalizable in a Fourier space (Davis 1979; Gray 2006). This allows us to solve the Poisson equation by means of a fast Fourier transform (FFT) method (Swarztrauber 1977; Soria, Pérez-Segarra & Oliva 2002) which decouples the initial system into N_{planes} mutually independent 2-D systems in the frequency space (frequency system). Therefore, the arithmetical complexity and the RAM memory of the problem are drastically reduced. Moreover, the independent 2-D systems are solved by means of a direct Schur-complement-based decomposition (DSD) method (Soria, Pérez-Segarra & Oliva 2003).

Concerning the parallelization strategy, initially each plane of the extrusion is divided into P_{2d} parts but, as all the planes are identical, the same partition is used for all of them. Consequently torus-shaped subdomains are obtained. Moreover, the azimuthal direction is also divided into P_{per} parts. Thus, the domain is decomposed into $P = P_{per} \times P_{2d}$ subdomains. When considering the optimal values for P_{per} and P_{2d}, the following two aspects must be taken into account: (i) the DSD method does not have unlimited speed-up, and thus, if P_{2d} overcomes the linear speed-up region, some resources may be wasted; (ii) when the change of basis to the diagonalization space is performed, a global communication between the processors assigned to different subdivisions of the torus-shaped subdomains is needed. The reason is that all the components of each azimuthal sub-vector are needed to perform the FFT. This global communication eventually degrades the parallelization when the number of partitions in the azimuthal direction, and consequently the number of processors involved in each global communication, increases. Thus, given a problem and a parallel computational architecture, some tests must be carried out in order to find out the optimal decomposition.

A study for determining the best option for solving the finest mesh ($74\,041 \times 128$ planes in the azimuthal direction) used in this paper has been performed. For this mesh size, 240 CPUs have been used in the simulation. In this case, the optimum parallelization strategy has been to divide the 2-D plane into 60 domains ($P_{2d} = 60$), while the azimuthal direction has been decomposed into four parts ($P_{per} = 4$). In absolute terms, the optimal time for solving the Poisson equation is 0.067 s, being about the 20 % of the total time required for computing one time step (0.337 s). All computations reported in this paper have been performed on a 76-node cluster, where each node has two AMD Opteron 2350 Quad Core processors linked in an infiniband DDR4X network.

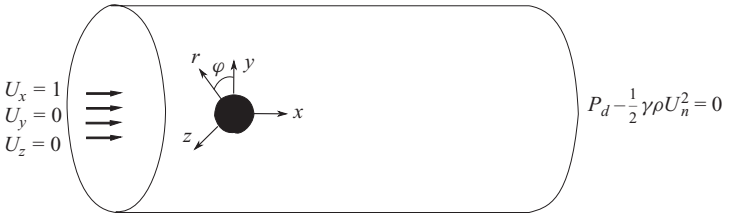

FIGURE 1. Computational domain and boundary conditions.

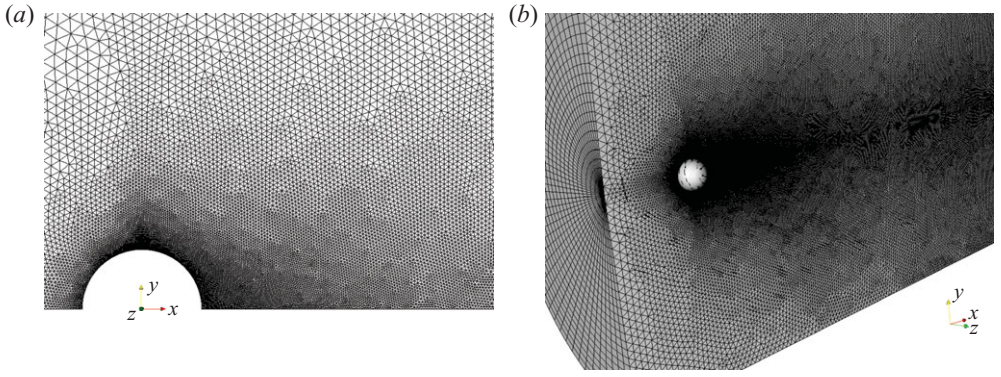

FIGURE 2. (Colour online available at journals.cambridge.org/FLM) (*a*) Details of the mesh of the 2-D grid in the region near the sphere and (*b*) 3-D mesh.

4. Flow parameters overview

Numerical simulations of the flow over a sphere have been performed at $Re = 3700$, where the Reynolds number ($Re = UD/\nu$) is defined in terms of the free-stream velocity U and the sphere diameter D. Solutions are obtained in a cylindrical computational domain of dimensions $x = [-5D, 20D]$; $r = [0, 7D]$; $\theta = [0, 2\pi]$, where the sphere is located at (0,0,0) (see figure 1). The boundary conditions at the inflow consist of a uniform velocity $(u, v, w) = (1, 0, 0)$. Constant velocity $(u, v, w) = (1, 0, 0)$ is also prescribed at the other external boundaries except for the downstream one (outlet) where a pressure-based condition is used. No-slip conditions on the sphere surface are imposed.

As mentioned in § 3, the governing equations are discretized on an unstructured mesh generated by the constant-step rotation around the axis of a 2-D unstructured grid. In this discretization, the azimuthal direction is divided into N_{planes} identical planes. The use of an unstructured grid for the plane has allowed us to cluster more CVs around the sphere and in the near wake. An example of the 2-D grid and its refinement around the sphere together with the 3-D mesh are depicted in figures 2(*a*) and 2(*b*) respectively. All the results presented in the paper have been performed on a grid of about 9.48 MCVs (74041×128 planes) which covers the whole domain.

When performing DNS, it must be ensured that the grid size is enough to solve the smallest flow scales well and that near the solid walls the viscous boundary layer is also well solved. This means that, within the boundary layer, a minimum number of grid points must be assured. Considering that the boundary layer is laminar until the drag crisis ($Re = 3.7 \times 10^5$) and that its thickness can easily be estimated Schlichting (1979), 12 grid points have been located within the boundary layer. Although the

grid used is unstructured, the mesh has been constructed to be as uniform as possible at the sphere surface and in the near wake. In the *a posteriori* analysis of the grid size used, the Kolmogorov length scale has been calculated. In the near wake, at a distance of up to $x/D < 3$, the minimum value of this length scale is given by $\eta/D = 0.0134$. This value increases up to $\eta/D = 0.0303$ at a distance of $x/D = 5$. The grid solved has an average grid size of $\overline{h}/D = 0.008$, with minimum values of $h_{min}/D = 0.0015$ in the zone behind the sphere up to $x/D = 3$, and $\overline{h}/D = 0.014$ for the region between $3 < x/D < 5$. With these considerations, the grid density obtained should be fine enough to solve the smallest flow scales in the zone behind the sphere and in the near wake up to a distance of $x/D = 10$ at this Reynolds number.

In the quest for an adequate grid resolution for solving the computational domain, three more different meshes of 5.45, 3.63 and 1.8 MCVs have been tested. For all these meshes, special care has also been taken in the node distribution near the sphere. Similar values of the drag coefficient and first-order statistics are obtained (see the Appendix). However, an accurate description of the Reynolds stresses and the unstable recirculation region needs the finest mesh.

5. Numerical simulation results

For obtaining the numerical results presented, small random disturbances have been introduced to the initially homogeneous flow field. At a certain time, the flow becomes 3-D and the transition to turbulence occurs in the wake of the sphere. Thus, simulation has been advanced in time until statistical stationary flow conditions have been achieved. Once the initial transient has been washed out, first- and second-order statistics have been obtained based on the integration of instantaneous data over a sufficiently long time period. In order to guarantee that the solved quantities are statistically independent, the evolution of first- and second-order statistics has been studied. A summary of these results is presented in figure 3. Figures 3(*a*) and 3(*b*) illustrate the time history averaging for streamwise (v_x) and radial velocity components (v_r), respectively. These values have been sampled at the axis at a distance of $x/D = 3$. This point is located downstream of the recirculation bubble, and at this station, the streamwise velocity exhibits clearly large fluctuations due to the turbulent mixing between the convected fluid along the shear layer and the fluid in the recirculation bubble. In the figure it can be observed how mean and turbulent statistics approach to converged values as time averaging increases. Based on these results, statistical data have been obtained by means of the integration of the instantaneous quantities over a period of 350 D/U time units. For this time integration period, the resolved turbulence statistics should be considered as statistically converged values. Furthermore, all statistical quantities have also been averaged in the azimuthal direction.

5.1. *Power spectra analysis*

The main frequencies corresponding to the shear-layer instabilities and large-scale vortex shedding have been obtained from the power spectrum analysis of the instantaneous data sampled at different stations in the near-wake region. The first of these probes is located at the axisymmetric shear layer at $x/D = 1.0$, $r/D = 0.6$. The second one is placed at $x/D = 2.4$, $r/D = 0.6$, in the zone of the shear layer where transition to turbulence is supposed to occur, the third one at $x/D = 3$, $r/D = 0.6$ and the last one at $x/D = 5$, $r/D = 0.6$ further downstream in the turbulent wake. The energy spectra have been calculated from the time series of the radial velocity

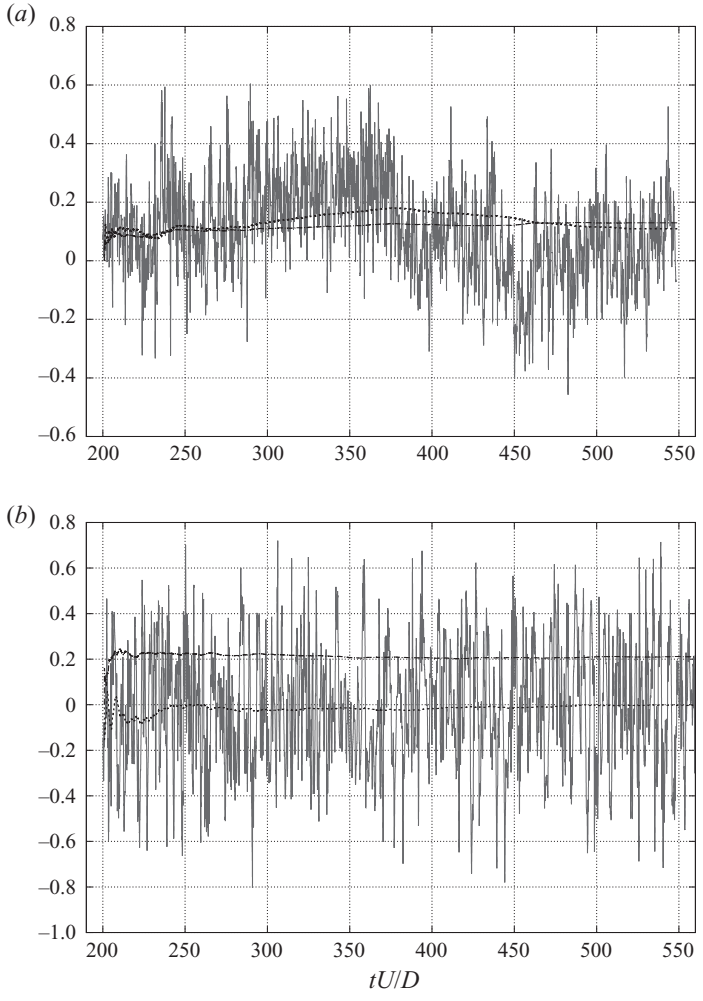

FIGURE 3. Time history for streamwise and radial velocity components and their time-averaging history: (*a*) streamwise velocity v_x (solid line), its time-average $\overline{v_x}$ (dotted line) and its time-averaged fluctuation $\overline{v_{x\,rms}}$ (dash-dotted line); (*b*) radial velocity v_r (solid line), its time-average $\overline{v_r}$ (dotted line) and its time-averaged fluctuation $\overline{v_{r\,rms}}$ (dash-dotted line).

fluctuations over a period of 350 tU/D (about 75 shedding cycles) by using the Lomb periodogram technique. In addition, the resulting spectra have been averaged in the azimuthal direction.

One can notice that radial velocity fluctuations display different frequency contributions depending on the position of the probes in the shear layer and in the wake. Indeed, the spectrum of the probe located at $x/D = 2.4$, $r/D = 0.6$ exhibits a dominant peak in the energy at the large-scale vortex-shedding frequency $S_t = f_{vs}\ D/U = 0.215$ (see figure 4*d*). This peak is also detected at all stations downstream of the sphere (figures 4*f* and 4*h*). The magnitude of the peak decreases slightly with the distance from the sphere, but it is clearly seen at all monitored ports. In the figures, the $-5/3$ Kolmogorov law is also represented. As can be seen from the figures, only at $x/D = 5$ does the slope of the spectrum approximate the $k^{-5/3}$ behaviour according to Kolmogorov's law for a narrow range of frequencies.

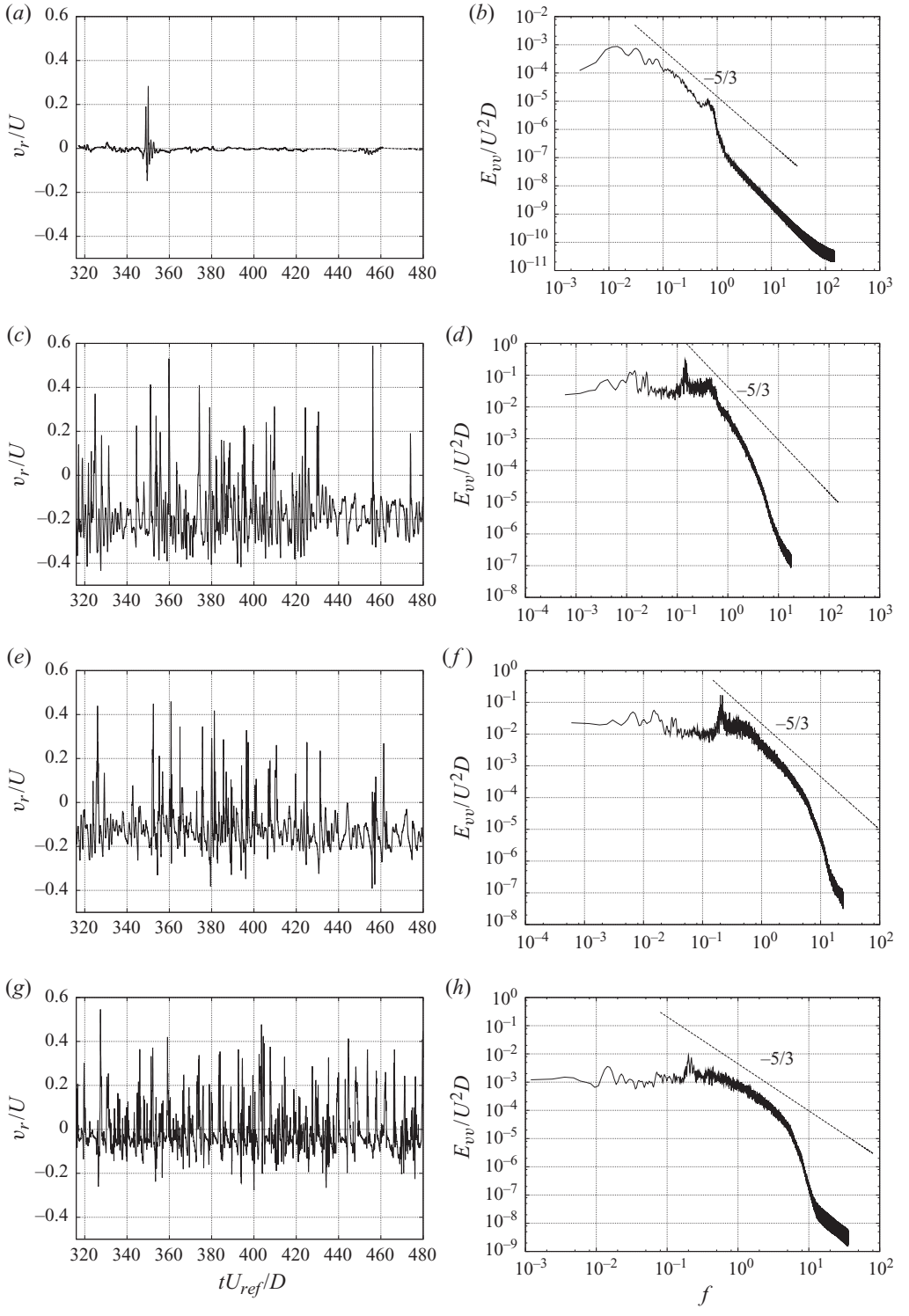

FIGURE 4. Time history and power spectrum at different locations: (*a*,*b*) radial velocity v_r and power spectrum at $x/D=1$, $r/D=0.6$, (*c*,*d*) radial velocity v_r and power spectrum at $x/D=2.4$, $r/D=0.6$, (*e*,*f*) radial velocity v_r and power spectrum at $x/D=3$, $r/D=0.6$, (*g*,*h*) radial velocity v_r and power spectrum at $x/D=5$, $r/D=0.5$.

However, at this low Reynolds number, the power spectrum almost passes directly from the energy carrying scales to the dissipative range.

In addition to the large-scale vortex-shedding frequency, there is a secondary characteristic frequency associated with the Kelvin–Helmholtz instabilities of the separating shear layer at $f_{KH}\ D/U = 0.72$. This frequency has been detected only in the very near wake, just downstream of the sphere (see the spectrum for the location $x/D = 2.4$, $r/D = 0.6$, figure 4*d*). In fact, the first probe located in the laminar region of the shear layer, closer to the separation point, also shows a broadband peak centred at f_{KH}. These instabilities can be observed as high-frequency fluctuations of the radial velocity, and they seem to grow in magnitude as the downstream distance from the sphere increases (see figures 4*a* and 4*c*, see also figure 8). Such intermittency has also been observed before for a circular cylinder by Prasad & Williamson (1997), who studied the shear layer instabilities, and has also been captured by DNS of the flow past a sphere at $Re = 650$ (Mittal & Najjar (1999) and at $Re = 1000$ (Tomboulides & Orszag (2000). In the experiments of the flow behind a sphere, this frequency has also been reported previously. Kim & Durbin (1988) reported a high-frequency mode to be between 0.75 and 1.04, while Sakamoto & Haniu (1990) measured a frequency value within 0.97–1.22. The value obtained in this paper is more consistent with the measurements of Kim & Durbin (1988), while there is little difference from that reported by Sakamoto & Haniu (1990).

Besides the vortex-shedding and the small-scale instability frequencies, another peak at a much lower frequency than that of the large-scale vortex shedding has been observed. The value of this low frequency is $f_m\ D/U = 0.0178$, and it is captured by all the probes. Tomboulides & Orszag (2000), who obtained a value of about $f_m\ D/U = 0.045$ at $Re = 500$, attributed this low frequency to the irregular rotation of the separation point. On the other hand, for the case of the wake of a circular disc, Berger, Cholz & Schumm (1990) found a periodic shrinkage and enlargement motion of the recirculation region at a very low frequency. If the energy spectrum of streamwise velocity fluctuations at $x/D = 3$, $r/D = 0$ shown in figure 3(*a*) is analysed (see figure 5), it also exhibits a dominant peak at a very low frequency of $f_m\ D/U = 0.0178$. This is the same low frequency found at the locations of the shear layer, especially at $x/D = 2.4$, $r/D = 0.6$ and at $x/D = 3$, $r/D = 0.6$. Just downstream of the recirculation bubble at $x/D = 3$, $r/D = 0.6$, it is expected to well capture this pumping motion of the recirculation zone. Thus, it is more probable that this low frequency (f_m) could be attributed to the periodic shrinkage and enlargement of the recirculation region than to the rotation of the vortex separation point.

5.2. *Coherent structures of the flow*

In order to understand the dynamics of the vortex formation and the wake structure, proper identification of the coherent structures of the flow is required. Thus, in the present work, coherent structures in the wake have been visualized by means of Q-iso-surfaces (see Hunt, Wray & Moin 1988). The Q-criterion proposed by Hunt *et al.* defines an eddy structure as a region with positive second invariant of the velocity gradient tensor $\boldsymbol{\nabla u}$. The second invariant is defined as

$$Q = \tfrac{1}{2}(\|\boldsymbol{\Omega}\|^2 - \|\boldsymbol{S}\|^2) \tag{5.1}$$

where $\|\boldsymbol{\Omega}\|^2 = [\mathrm{Tr}(\boldsymbol{\Omega}\boldsymbol{\Omega}^t)]$ and $\|\boldsymbol{S}\|^2 = [\mathrm{Tr}(\boldsymbol{S}\boldsymbol{S}^t)]$, $\boldsymbol{\Omega}$ and $\boldsymbol{S}$ being the antisymmetric and symmetric components of the velocity gradient tensor $\boldsymbol{\nabla u}$. Positive values of Q mean that vorticity prevails over strain, i.e. the strength of rotation overcomes the strain.

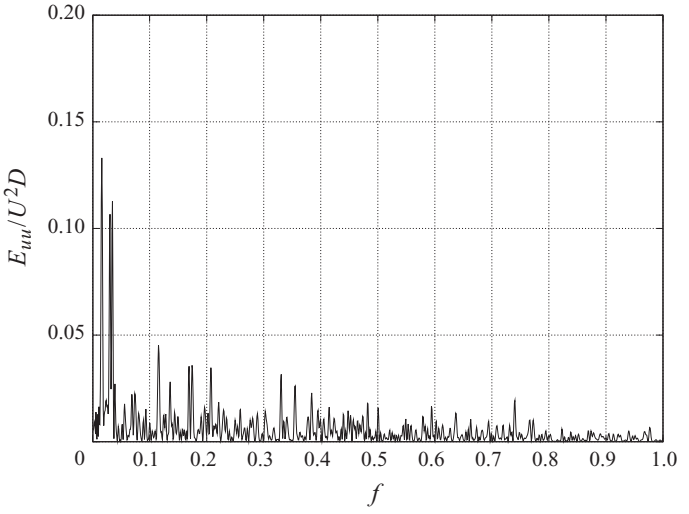

FIGURE 5. Power spectrum of the streamwise velocity fluctuations v_x' at $x/D = 3$, $r/D = 0$.

In figures 6 and 7, a sequence of four Q-iso-surface plots is presented. This sequence corresponds with the time evolution of the vortical structures in the wake of the sphere over a shedding cycle, viewed from two different azimuthal positions. Each panel of the figures depicts the wake of the sphere at each quarter period. Figure 6 corresponds to an arbitrary azimuthal position (e.g $X-Y$ plane) and figure 7 is perpendicular to the $X-Y$ plane, viewed from the top.

An axisymmetric laminar boundary layer separates from the equator of the sphere, with a separation angle of $\varphi_s = 89.5^\circ$. This separated shear layer remains laminar up to a certain distance from the sphere where it becomes unstable. From the analysis of the instantaneous data, it has been observed that at about $x/D = 1$–1.2, the first instabilities in the shear layer appear. These instabilities occur, in the first instance, as a consequence of the amplification of the small random disturbances introduced in the initial conditions. Due to these instabilities in the shear layer that appear randomly at any azimuthal location, the vortex sheet starts to roll up, and the flow becomes 3-D and results in a transition to turbulence. The zone where this transition occurs is located at about $x/D = 1.8$–2.6. The instabilities in the shear layer can be directly seen from the inspection of the time series of the radial velocity component in the laminar shear layer at $x/D = 1$, $r/D = 0.6$ at four azimuthal angles ($\theta = 0$, $\pi/2$, π, $3\pi/2$) (see figure 8a). As can be observed, large velocity fluctuations occur randomly at all azimuthal positions but at different times. These instabilities propagate in the shear layer and get amplified. As a consequence, in the zone where the transition to turbulence occurs, large velocity fluctuations are found at every azimuthal angle as shown in figure 8(b) ($x/D = 2.2$, $r/D = 0.6$).

As can be seen from figures 6 and 7, there is a wide range of scales in the separated region, just behind the recirculation bubble and in the wake of the sphere. Vortex loops are detached from opposite positions, but they are not necessarily detached with 180° of separation. In the separated zone, the vortices formed break into small-scale vortices which are drawn into the region behind the sphere (formation zone), but they also feed the turbulent wake. The large-scale vortices are not arranged in the same plane, but the wake exhibits a pronounced helical-like configuration as can also be observed from the general 3-D view of the wake in figure 9. This helical configuration

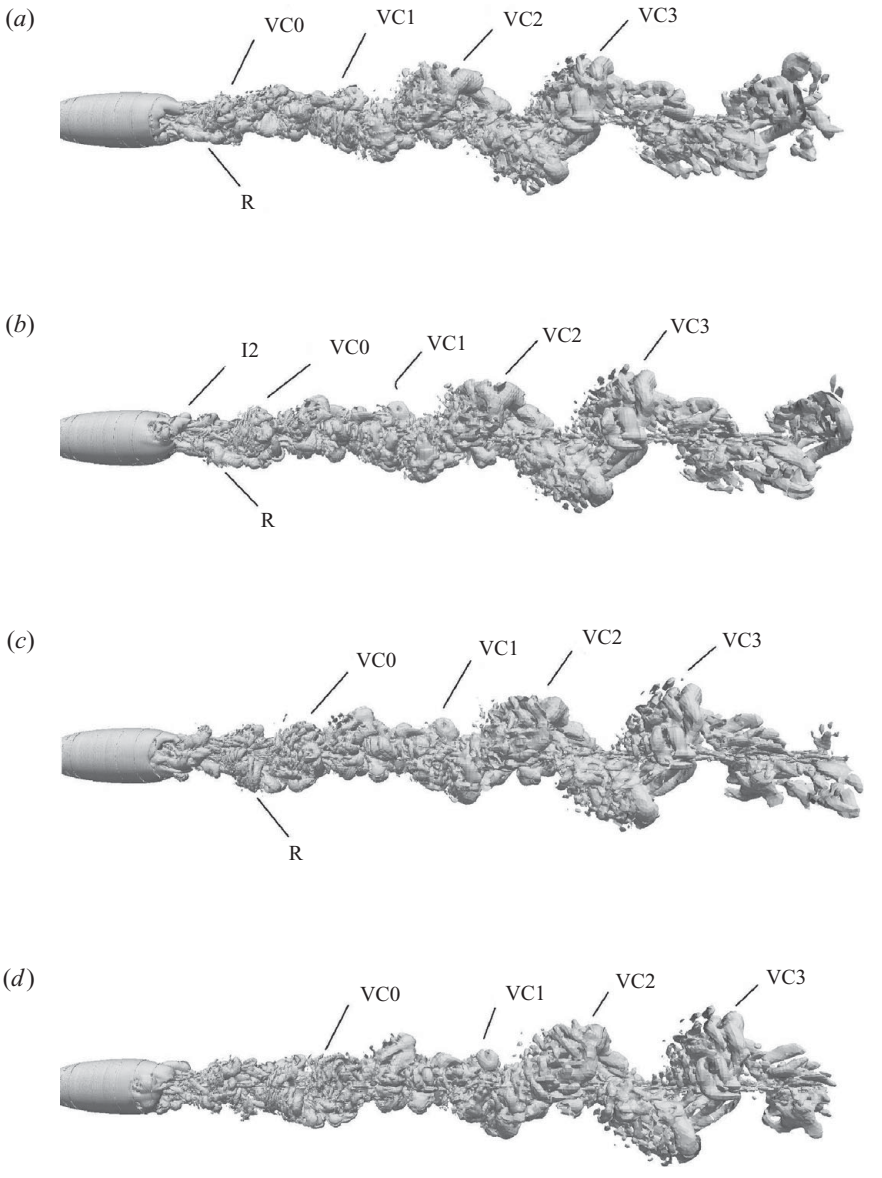

FIGURE 6. Vortical structures every quarter vortex-shedding period (time advances from *a* to *d*). Plane $X-Y$.

was previously observed in experiments carried out by Achenbach (1974) at $Re = 6000$ and by Taneda (1978) at $Re = 10^4$–3.8×10^5, and in numerical results at $Re = 10^4$ (see Constantinescu & Squires 2004; Yun *et al.* 2006). In his experimental observations, Achenbach (1974) suggested that the vortex shedding occurs at a position around the sphere that rotates with the vortex-shedding frequency. On the other hand, Taneda (1978) observed an irregular rotation about the axis of the separation point and the wake. However, recent LES results from Yun *et al.* (2006) showed that vortical structures travel downstream nearly straight, and they proposed that the helical-like structure might be related to the wall-pressure changes in the sphere along the azimuthal direction.

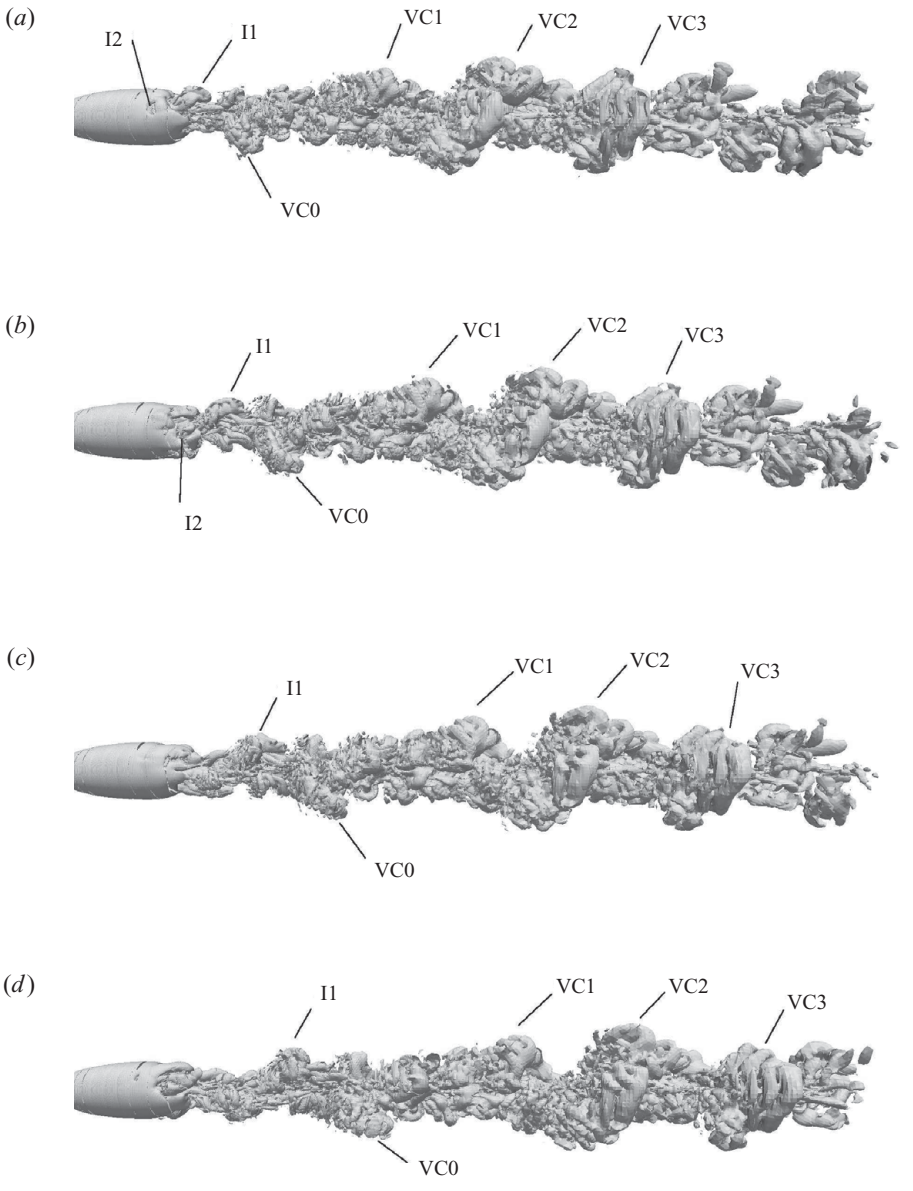

FIGURE 7. Vortical structures every quarter vortex-shedding period (time advances from *a* to *d*). Plane perpendicular to the $X-Y$ plane, viewed from the top.

From the examination of a large number of shedding cycles of the instantaneous data in the present simulation, it has been observed that shear layer instabilities occur at a random position and the vortices are shed periodically at no particular azimuthal position. This gives the wake a helical appearance but the vortices move downstream without circulation in the azimuthal direction (see the supplementary movie available at journals.cambridge.org/flm). In fact, it can be argued that the observed helical pattern of the wake is due to the way the vortices are shed in time. At any shedding cycle, two antisymmetric vortices are shed, but at the next shedding period, due to the randomness of the shear layer instabilities, the vortex shedding does not occur at

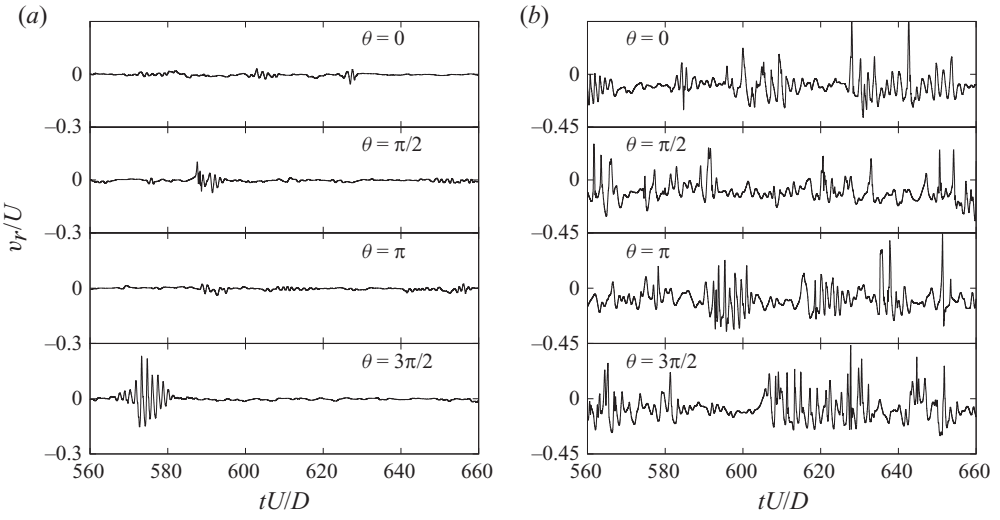

FIGURE 8. Time series of the radial velocity component at different locations in the shear layer and at four azimuthal angles ($\theta = 0,\ \pi/2,\ \pi,\ 3\pi/2$): ($a$) $x/D = 1$, $r/D = 0.6$; (b) $x/D = 2.2$, $r/D = 0.6$.

the same azimuthal position as that of the previous one. Instead, these perturbations can produce vortices to be shed either to the left or to the right of the location of the previous vortex shedding. Thus, the handedness of the helical pattern is determined (in the first instance) by the amplification of the random disturbances introduced in the initial conditions, but also the direction of the helix will vary in time due to the nature of the vortex-shedding process.

Analysing the shedding cycle shown in the figures, panels 6(a) and 7(a) depict the shear layer in a stage just after the instability marked as I1 has grown and has broken off from the vortex sheet. Small instabilities in the axisymmetric shear layer are continuously appearing (e.g. the instability marked as I2). At the end of the axisymmetric bubble, corrugated structures along the azimuthal direction can also be observed. These structures are induced by the action of the small scales inside the recirculation bubble and the remnants of the previous ones broken off from the shear layer. A protruding structure marked as VC0, which is the previous separated roller on the opposite side of the shear layer, and other vortices marked as VC1, VC2 and VC3 can also be noted. Figures 6(b) and 7(b) correspond to a quarter period later when the structure I1 has become amplified and moved downstream. Of particular interest is the long-rib structure (R) which is connected at one end with the VC0 structure. The corrugated structures at the end of the vortex sheet are now more evident, as instability I2 has completely broken the shear layer at that azimuthal position. In the top view, small streamwise vortices which seem to be interlaced with the vortex structure I1 can also be observed.

A quarter period later, which corresponds with figures 6(c) and 7(c), the vortex structure I1 has completely separated from the shear layer. The tail of the rib R has distorted in the azimuthal direction and has wrapped around itself, feeding the VC0 vortex, which has grown also fed by the small-scale vorticity from the recirculation bubble. The instability I2 has now separated from the shear layer and has grown as a new vortex structure opposite to I1. In the last quarter (figures 6d and 7d), the vortex structure I1 has moved downstream, while the new vortex shed I2 is now in its

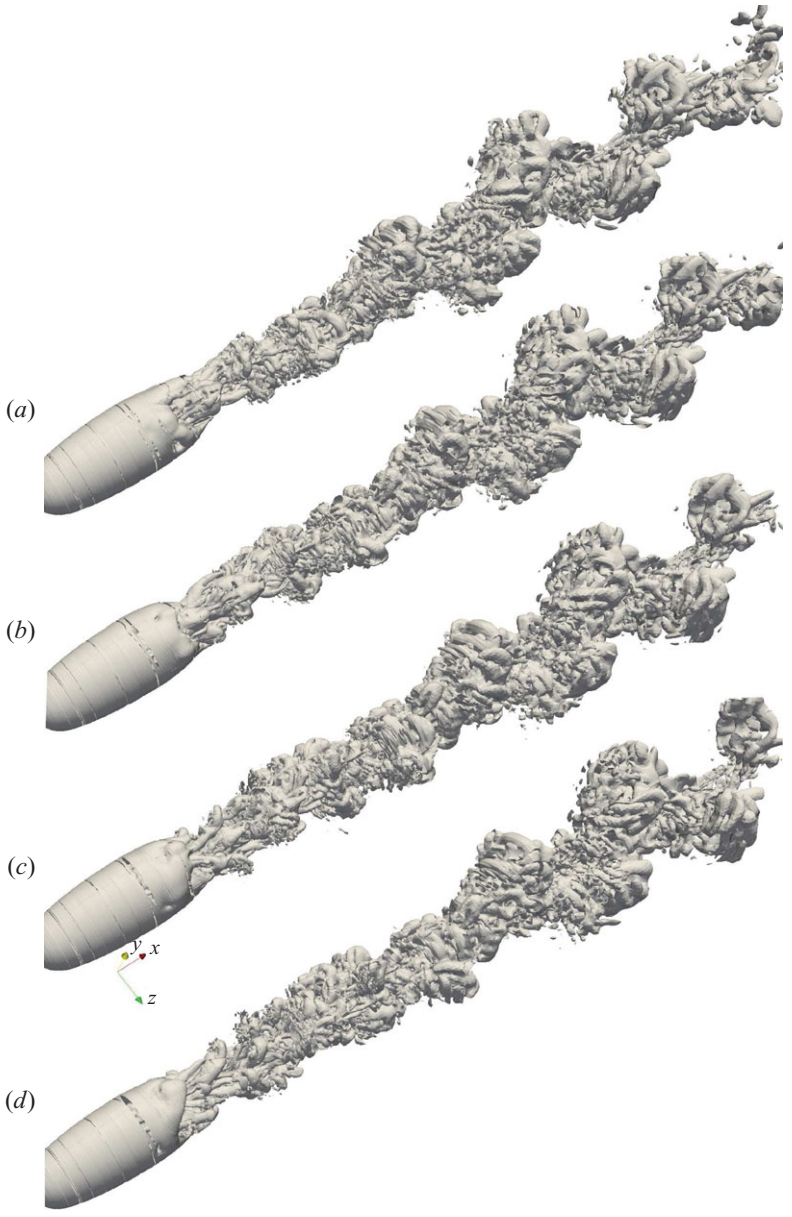

FIGURE 9. (Colour online) Visualization of instantaneous vortical structures in the wake of the sphere (time advances from a to d).

final stage. Moreover, as a consequence of the pairing of vortices, VC0 has become a larger structure.

The same shedding period shown in figures 6 and 7 is also depicted in figure 9, but it offers a 3-D view of the helical pattern of the wake. Note also that large-scale structures are composed of about 3–4 azimuthal vortex rings, which is in agreement with the small-scale instability frequency f_{KH} measured. During the whole sequence, the large-scale structures such as VC1, VC2 and VC3 have moved uniformly

	Re	S_t	φ_s (°)	$\overline{C_d}$	$\overline{C_{pb}}$	L/D
Present work (DNS)	3700	0.215	89.4	0.394	−0.207	2.28
Kim & Durbin (1988) (exp.)	3700	0.225	–	–	−0.224	–
Sakamoto & Haniu (1990) (exp.)	3700	0.204	–	–	–	–
Yun *et al.* (2006) (LES)	3700	0.21	90	0.355	−0.194	2.622
Schlichting (1979) (exp.)	3700	–	–	0.39	–	–
Tomboulides & Orszag (2000) (DNS)	1000	0.195	102	–	–	1.7
Seidl *et al.* (1998) (DNS)	5000	–	89.5	0.38	–	2.1
Constantinescu & Squires (2003) (LES)	10^4	0.195	84–86	0.393	–	1.7

TABLE 1. Statistical flow features. DNS results compared with experimental measurements and numerical results from the literature.

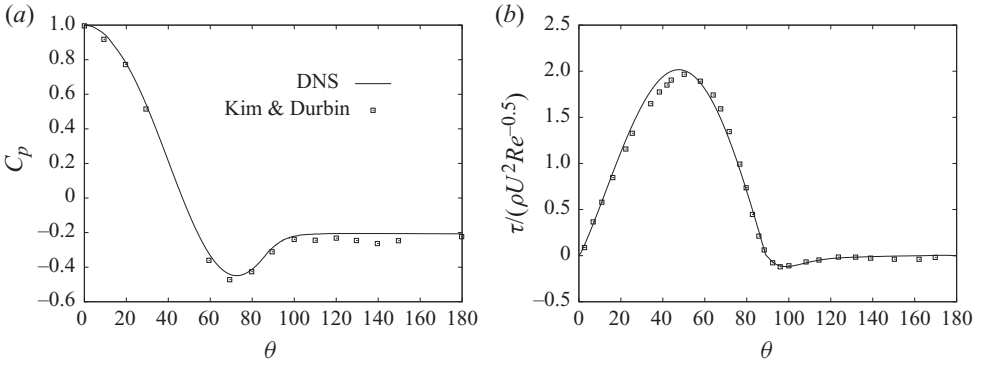

FIGURE 10. Mean profiles around the sphere. (*a*) Mean pressure distribution compared with experimental results of Kim & Durbin (1988) at $Re = 4200$. (*b*) Mean skin-friction coefficient compared with numerical results of Seidl *et al.* (1998) at $Re = 5000$.

downstream without change in their azimuthal position. As they travel downstream, the whole wake gives the appearance of a wavy motion and, as has been commented before, it exhibits this helical-like configuration.

5.3. *First- and second-order statistics*

Time-averaged statistical features resulting from the simulation are summarized in table 1. In the table, the vortex-shedding frequency, S_t, the separation angle measured from the stagnation point, φ_s, the non-dimensional length of the recirculation bubble evaluated from the rear end of the sphere, L/D, and the mean streamwise drag coefficient, $\overline{C_d}$, are presented. Previous numerical results and experimental data from the literature are also given. In general, good agreement with previous data has been found for all time-averaged flow features.

As commented in § 5.1, vortices are shed from the sphere at a frequency $S_t = 0.215$. This value is within the range (0.204–0.225) of Strouhal numbers reported in experiments (see Kim & Durbin 1988; Sakamoto & Haniu 1990), as can be seen in the table.

Predictions of the angular distribution of the mean pressure coefficient, $\overline{C_p}$, and the wall skin-friction, τ_w, are plotted in figure 10 against the results from the literature at comparable Reynolds numbers. As experimental measurements of the drag coefficient (see values summarized in Schlichting 1979) have shown little variation in this quantity in the sub-critical regime, the dependence on the Reynolds number is not so important.

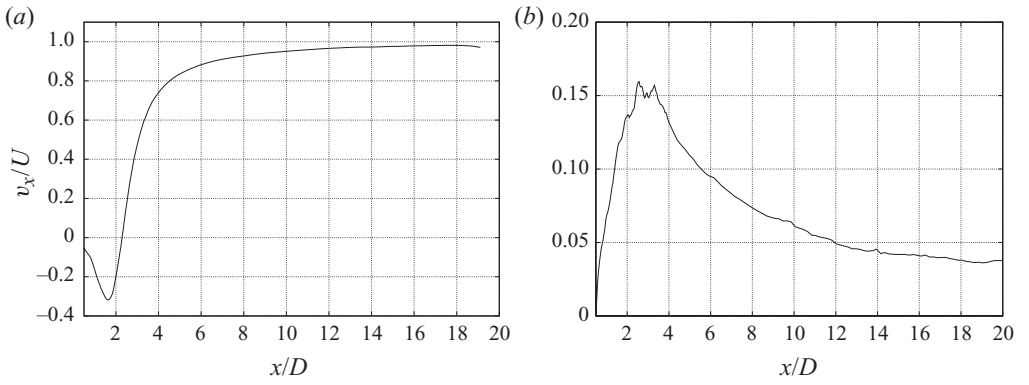

FIGURE 11. (*a*) Time-averaged streamwise velocity ($\overline{v_x}$) profile along the wake centreline. (*b*) Mean fluctuating streamwise velocity ($\overline{v_x'}$) along the wake centreline.

Thus it is possible to carry out comparisons with other results from the literature at different Reynolds numbers. In figure 10(*a*), the mean pressure coefficient is compared against earlier experimental measurement data of Kim & Durbin (1988) at $Re = 4200$. As can be seen, when comparing the DNS results with those obtained from Kim & Durbin (1988), good agreement within experimental uncertainties is obtained. The angular position of the pressure minimum is well captured, being at $\varphi = 71.5°$. This value is also comparable with the position of the pressure minimum, $\varphi = 71°$, reported by Seidl *et al.* (1998) at $Re = 5000$. The value of the base pressure coefficient $\overline{C_{pb}}$, i.e. the time-mean pressure coefficient at the rear point of the sphere at $\varphi = 180°$, is also well predicted (see table 1).

The skin-friction distribution obtained and the DNS results of Seidl *et al.* (1998) at $Re = 5000$ are depicted in figure 10(*b*). The values presented have been non-dimensionalized by $\rho U^2/Re^{0.5}$ being consistent with the boundary layer theory. The variation of the skin-friction coefficient with the angle is also in correspondence with previous results. As can be observed, it exhibits a maximum value at the angular position of $\varphi = 48°$, which compares well with the value calculated by Seidl *et al.* (1998) of $\varphi = 50°$.

As shown in table 1, the value of the mean drag coefficient, $\overline{C_d} = 0.394$, is in correspondence with the value reported in experiments, $\overline{C_d} = 0.39$ (values summarized in Schlichting 1979). This is also in agreement with the observations that report a local minimum of the drag coefficient of $\overline{C_d} = 0.38$ at about $Re = 5000$ (see Seidl *et al.* 1998) with the further increase with the Reynolds number in the sub-critical regime approaching the drag crisis (Schlichting 1979; Constantinescu & Squires 2003). However, when compared with the LES results by Yun *et al.* (2006), some discrepancies are found. They predicted a lower value for the drag coefficient of $\overline{C_d} = 0.355$. It is important to highlight that computations performed with coarser grids of 3.63 MCVs and 5.45 MCVs have shown little variation in the value of the mean drag coefficient $\overline{C_d}$ being 0.39 and 0.399, respectively. Thus, differences with LES results might be attributed to the subgrid-scale model they have used.

The average streamwise velocity ($\overline{v_x}$) normalized by the free-stream velocity U and its fluctuations ($\overline{v_x'}$) are given in figure 11. As can be seen from figure 11(*a*), the length of the recirculation bubble, defined as the streamwise distance from the rear end of the sphere to the position where the mean streamwise velocity changes sign, is $L/D = 2.28$. This is nearly the same distance to the location where the fluctuations of

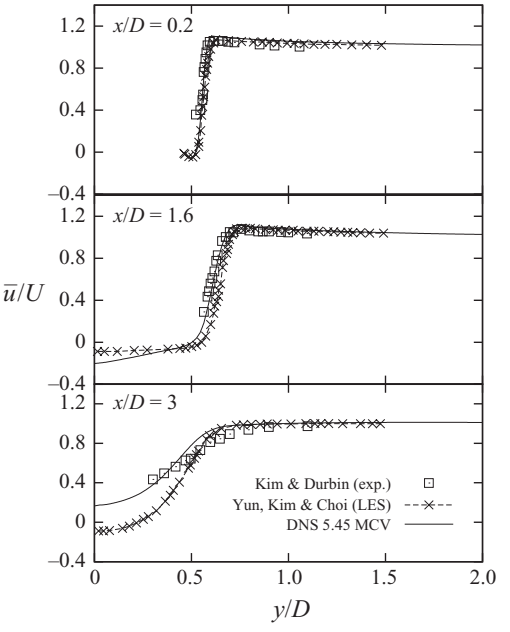

FIGURE 12. Streamwise velocity at three locations in the wake. Comparison of the DNS results with experiments of Kim & Durbin (1988) and LES solution of Yun *et al.* (2006).

the streamwise velocity reach its maximum, i.e. the vortex formation zone, as Norberg (1998) pointed out. In fact, figure 11(*b*) shows the presence of two large peaks. The first one is more pronounced and its maximum occurs at $x/D = 1.98$ measured from the rear end of the sphere, while the second one takes place at $x/D = 2.81$. Some discrepancies with the previous LES modelling work by Yun *et al.* (2006) are observed in the prediction of the recirculation length (see table 1). These differences are also reflected when the profile of the mean streamwise velocity in the wake is compared with both experimental data of Kim & Durbin (1988) and LES modelling results by Yun *et al.* (2006) (see figure 12). Good agreement between our DNS results and the experimental data is obtained. However, noticeable differences are observed when compared with the mentioned LES results. These discrepancies are more relevant at $x/D = 3$ where, according to our DNS and the experimental measurements, the flow is in the recovery zone (i.e. the region between the end of the recirculation bubble and the location where the flow accelerates in spite of the adverse pressure gradient). However, for LES results by Yun *et al.* (2006), the profile shows that the flow is at the end of the recirculation bubble.

The time-averaged profiles of the streamwise and radial velocities at five different locations ($x/D = 1.6$, 2, 3, 5, 10) in the wake are plotted in figure 13. The negative streamwise velocity at $x/D = 1.6$ and 2 stems from the recirculation zone. In the wake behind the sphere, $\overline{v_x}$ is negative until the free-stagnation point. At $x/D = 3$, the streamwise velocity is positive but near zero, since this position is very close to the end of the recirculation bubble. The minimum value of the radial velocity occurs on the side of the free-stagnation point, and its value is $\overline{v_r} = -0.198\,U$ (see table 2). The largest backward velocity (minimum streamwise velocity) in the recirculation bubble is $\overline{v_x} = -0.321\,U$ according to figure 11(*a*).

The mean velocity fluctuations $\overline{v_x'}/U$ and $\overline{v_r'}/U$ are plotted in figure 14. The averaged maps of the Reynolds stresses $\overline{v_x'v_x'}/U^2$, $\overline{v_r'v_r'}/U^2$ and $\overline{v_x'\,v_r'}/U^2$ are also

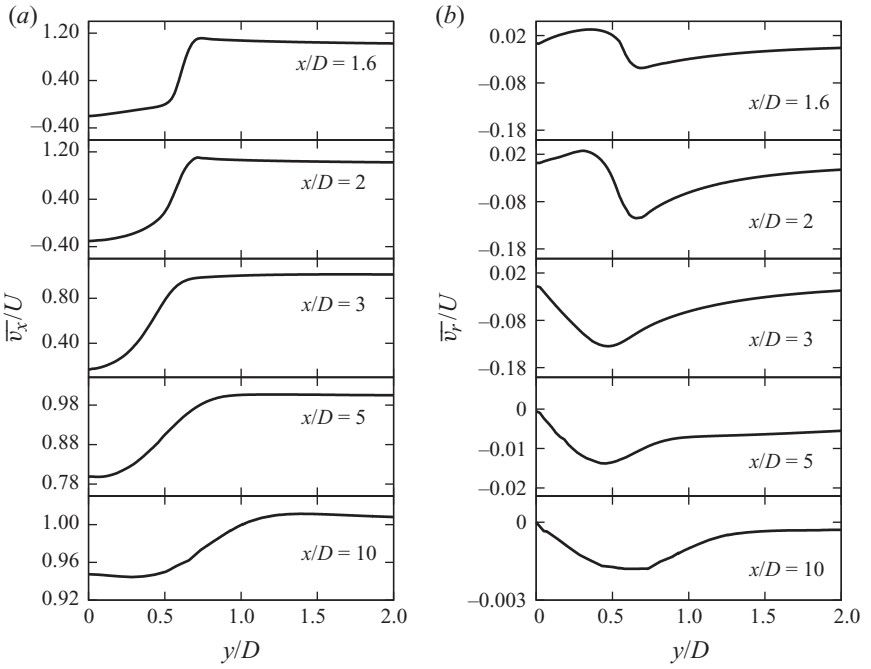

FIGURE 13. Mean velocity profiles at different positions in the wake behind the sphere at the plane $(x/D, y/D, z=0)$. (a) Streamwise velocity $\overline{v_x}/U$, (b) radial velocity $\overline{v_r}/U$.

depicted in figure 15. The contour plots show qualitative agreement with particle image velocimetry (PIV) measurements of Jang & Lee (2007) for a Reynolds number $Re = 11\,000$. As expected, low levels of the Reynolds stresses in the near wake, in the region close to the sphere, are observed. On the contrary, peaks in the stresses are within a distance of $1.8D$–$2.5D$ from the sphere. The largest streamwise turbulence intensity is located at $x/D = 2.61$ around which contours are arranged in the recirculation zone. In fact, the largest values of this variable occur in the shear layer at a radial position around $0.4 \leqslant r/D \leqslant 0.6$ (see figures 14*a* and 15*a*). Furthermore, the maximum value of the cross-stream Reynolds stresses $\overline{v_r' v_r'}/U^2$ occurs along the wake centreline at $x/D = 3.1$ (see figures 14*b* and 15*b*). All these representative quantities are summarized and compared (when possible) with the LES results by Constantinescu & Squires (2003) at $Re = 10^4$, in table 2. Although there is a difference in Reynolds numbers, note that the minimum/maximum values of these variables take place at nearly the same radial location, but the streamwise position is larger in our calculations. These differences in the axial position are attributed to the shrinkage of the recirculation bubble with the increase in the Reynolds number.

6. Summary

The direct numerical simulation of the flow over a sphere has been carried out at the Reynolds number of $Re = 3700$. A second-order spectro-consistent scheme for collocated and unstructured grids is used in the discretization of the governing equations. The conservation properties ensure good stability and conservation of the kinetic-energy balance with coarse meshes even at high Reynolds numbers. The

	Value	x/D	y/D
Minimum mean streamwise velocity $\overline{v}_x/U$			
DNS	−0.321	2.133	0.0
LES, $Re=10^4$	−0.4	1.41	0.0
Maximum mean streamwise velocity $\overline{v}_x/U$			
DNS	1.175	1.282	0.702
LES, $Re=10^4$	–	–	–
Minimum mean radial velocity $\overline{v}_r/U$			
DNS	−0.198	2.499	0.572
LES, $Re=10^4$	−0.15	1.82	0.56
Maximum mean radial velocity $\overline{v}_r/U$			
DNS	0.207	0.0014	0.565
LES, $Re=10^4$	–	–	–
Maximum mean streamwise turbulent intensity $\overline{v'_x\,v'_x}/U^2$			
DNS	0.055	2.606	0.423
LES, $Re=10^4$	0.063	1.78	0.46
Maximum mean radial turbulent intensity $\overline{v'_r\,v'_r}/U^2$			
DNS	0.069	3.090	0.0
LES, $Re=10^4$	–	–	–
Minimum mean Reynolds shear stress $\overline{v'_x\,v'_r}/U^2$			
DNS	−0.029	2.565	0.392
LES, $Re=10^4$	−0.039	2.04	0.39

TABLE 2. First- and second-order statistics. Comparison with LES results of Constantinescu & Squires (2003) at $Re=10^4$.

results have been computed on an unstructured grid of about 9.48 MCVs generated by the constant-step rotation around the axis of a two-dimensional unstructured grid. Time-averaged statistics have been based on the integration of the instantaneous statistical stationary data over a period of 75 vortex-shedding cycles and also spatially averaged in the periodic direction.

The computed results have been compared with experimental and numerical data available in the literature at comparable Reynolds numbers. It has been found that the flow separates laminarly near the equator of the sphere and transition to turbulence occurs in the separated shear layer at a distance between $x/D=1.8$ and 2.6. The flow parameters, such as vortex-shedding frequency, instability frequency, drag coefficient and detachment angle, have been found to be consistent with previous works. Good agreement in the wall-pressure and skin-friction distributions in the sphere has also been found.

The energy spectra of a set of selected probes at different locations in the wake of the sphere have been calculated. The spectra exhibit different frequency contributions depending on the position of the probes. Three main instability frequencies have been detected: the large-scale vortex-shedding frequency at $S_t=f_{vs}\,D/U=0.215$; the small-scale Kelvin–Helmholtz instability of the shear layer at $f_{KH}=0.72$; and a frequency lower than the vortex-shedding frequency attributed to the shrinkage and enlargement of the recirculation region at $f_m=0.0178$. The vortex-shedding frequency and the Kelvin–Helmholtz instability have been found to be in good agreement with previous studies.

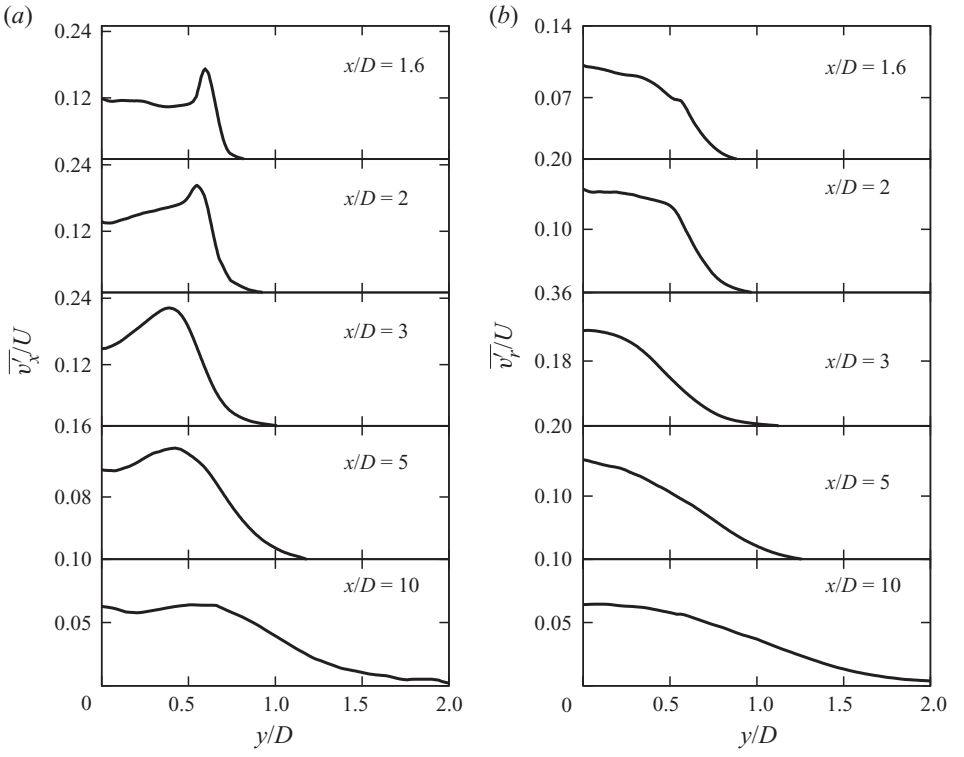

FIGURE 14. Mean velocity fluctuations at different positions in the wake behind the sphere at the plane $(x/D, y/D, z=0)$. (*a*) Streamwise velocity fluctuations $\overline{v_x'}/U$, (*b*) radial velocity fluctuations $\overline{v_r'}/U$.

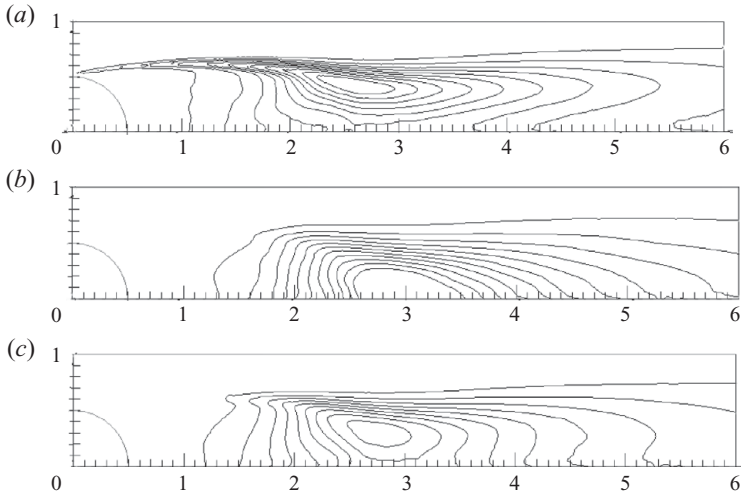

FIGURE 15. Isocontour maps of the second-order statistics: (*a*) Reynolds streamwise normal stress $\overline{v_x' v_x'}/U^2 = 0.00552$–$0.0554$, 10 levels. (*b*) Reynolds cross-stream normal stress $\overline{v_r' v_r'}/U^2 = 0.00685$–$0.0685$, 10 levels. (*c*) Reynolds shear stress $\overline{v_x'\, v_r'}/U^2 = -0.029$–$0.00323$, 10 levels.

Case	N_t(MCV)	$N_{CVplane}$	N_{planes}	N_{BL}
I	9.48	74 041	128	12
II	5.45	56 787	96	10
III	3.63	56 787	64	8
IV	1.8	28 168	64	4

TABLE 3. Main parameters for the different computations. N_t, total number of CVs; $N_{CVplane}$, number of CVs in the plane; N_{planes}, number of planes in the azimuthal direction; N_{BL}, number of points in the viscous boundary layer.

The visualization of the vortex structures over a long period of time shows that the wake has a marked helical-like configuration due to the shedding of vortices at random azimuthal positions in the shear layer. Although during a vortex-shedding period coherent structures are antisymmetric, vortex loops are not strictly detached with 180° of separation. Furthermore, as every vortex-shedding period does not occur at the same circumferential location and there is a random change in its azimuthal position, vortices are shed either to the left or to the right of the location of the previous one. However, large-scale structures move uniformly downstream without circulation in the azimuthal direction, but their relative positions give the appearance of a wavy motion and helical configuration.

In addition to the flow parameters presented, a detailed set of first- and second-order statistics at different positions in the wake have also been given. As far as the authors are aware, this work presents the first DNS carried out at this Reynolds number. Furthermore, the data obtained are useful not only for a better understanding of the flow features but also for assessing and validating the results from turbulence modelling.

It is worth highlighting that the methodology developed for solving bodies of revolutions using unstructured grids has allowed us to accurately solve the flow in the wake of the sphere with good results. Furthermore, the computational cost of the present computations is relatively small for the grids used, which allows us to carry out similar DNS studies at higher Reynolds numbers.

This work has been financially supported by the Ministerio de Educación y Ciencia, Secretaría de Estado de Universidades e Investigación, Spain (ref. ENE2009-07689) and by the Collaboration Project between Universitat Politècnica de Catalunya and Termo Fluids SL (ref. C06650). The authors would also like to thank the referees for their useful comments, which served to improve the paper.

Appendix. Grid resolution studies

We performed simulations with different resolutions in both the 2-D plane (x, r) and the azimuthal direction. The coarser mesh solved was of 1.8 MCVs (28168×64 planes). In all cases a minimum number of CVs within the boundary layer were considered (4 CVs for the coarse grid and 12 CVs for the finest one). Mesh refinement was carried out taking advantage of the unstructured grids used. Thus, more CVs were clustered within the near-wake region than in the outer zones where the flow is laminar. Table 3 summarizes the details of each computational grid considered.

Flow features resulting from the different simulations are given in table 4. In all cases, statistical data were obtained by averaging 350 D/U time units. The drag

	S_t	φ_s (°)	$\overline{C_d}$	$\overline{C_{pb}}$	L/D
Case I (9.48 MCV)	0.215	89.4	0.394	−0.207	2.28
Case II (5.45 MCV)	0.215	89.4	0.399	−0.209	2.18
Case III (3.63 MCV)	0.21	89.35	0.390	−0.238	2.08
Case IV (1.8 MCV)	0.215	89.5	0.378	−0.234	2.35
Kim & Durbin (exp.)	0.225	–	–	−0.224	–
Sakamoto & Haniu (exp.)	0.204	–	–		–
Yun *et al.* (LES)	0.21	90	0.355	−0.194	2.622

TABLE 4. Statistical flow parameters for the different grids. Experimental measurements from Kim & Durbin (1988) and Sakamoto & Haniu (1990), and numerical results from LES computations by Yun *et al.* (2006).

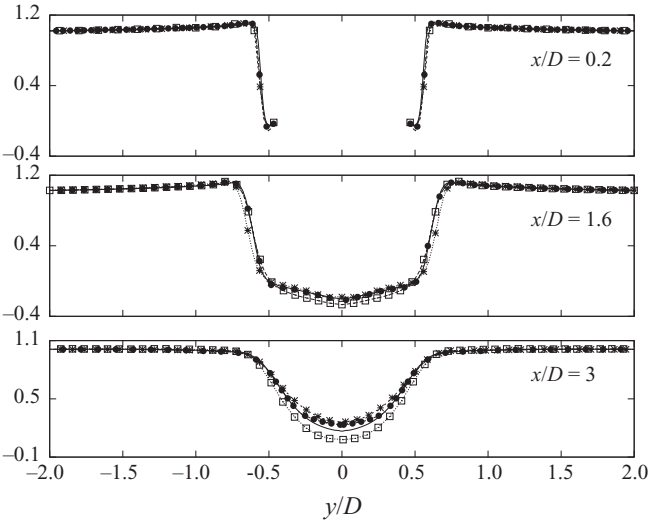

FIGURE 16. Streamwise velocity profiles at different locations in the near wake of the sphere for different grid resolutions: —, case I; ●, case II; ∗, case III; □, case IV.

coefficient $\overline{C_d}$, the base pressure coefficient $\overline{C_{pb}}$, the vortex-shedding frequency S_t and the separation angle φ_s agree quite well with the experimental data for all resolutions. On the other hand, the recirculation length shows a higher sensitivity to the grid resolution. These differences are also reflected in the mean streamwise velocity profiles in the near wake (see figure 16). Good agreement is obtained at $x/D = 0.2$ and $x/D = 1.6$, but some differences are observed when they are compared at a distance of $x/D = 3$. As this station is located at the outer limit of the recirculation zone, these differences might be due to the fluctuations of the recirculation bubble. Largest differences in the mean flow variables are obtained in the downstream region when compared with the high-resolution mesh, specially for the two coarser grids, for downstream distances from the sphere of $x/D > 5$ (not shown in the image). These differences are mainly due to the coarsening of these grids further downstream, being incapable of capturing all flow scales.

Figure 17 shows the mean pressure coefficient on the sphere surface as a function of the angle (measured from the stagnation point) for the low- and high-resolution grids (cases IV and I, respectively), together with the experimental data by Kim & Durbin

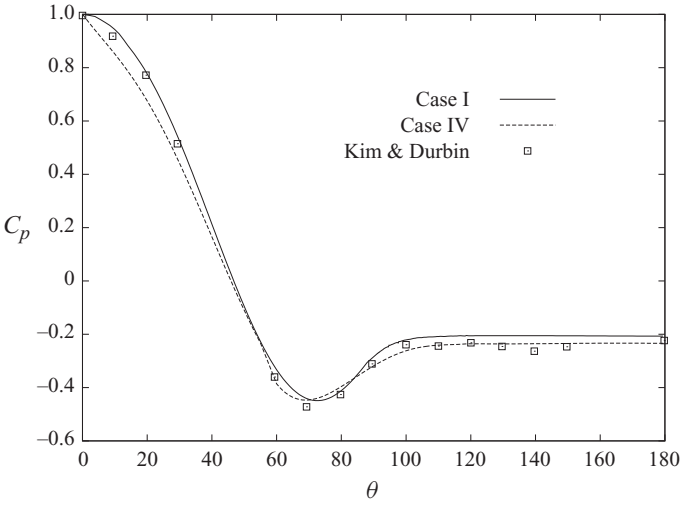

FIGURE 17. Comparison of the pressure coefficient on the sphere surface: —, case I; - - -, case IV; □, experimental data by Kim & Durbin (1988).

(1988) at $Re = 4200$. The low-resolution mesh captures the pressure distribution quite well with some differences in the front surface of the sphere, and also it slightly under-predicts the pressure in the base of the sphere. However, the position of the minimum pressure and its value are predicted satisfactorily.

REFERENCES

ACHENBACH, E. 1972 Experiments on the flow past spheres at very high Reynolds numbers. *J. Fluid Mech.* **54**, 565–575.

ACHENBACH, E. 1974 Vortex shedding from spheres. *J. Fluid Mech.* **62** (2), 209–221.

BAKIC, V., SCHMID, M. & STANKOVIC, B. 2006 Experimental investigation of turbulent structures of the flow around a sphere. *Intl J. Therm. Sci.* **10** (2), 97–112.

BERGER, E., CHOLZ, D. & SCHUMM, M. 1990 Coherent vortex structures in the wake of a sphere and a circular disk at rest and under forced vibrations. *J. Fluids Struct.* **4** (3), 231–257.

CONSTANTINESCU, G. & SQUIRES, K. 2003 LES and DES investigations of turbulent flow over a sphere at $Re = 10000$. *Flow Turbul. Combust.* **70**, 267–298.

CONSTANTINESCU, G. & SQUIRES, K. 2004 Numerical investigations of flow over a sphere in the subcritical and supercritical regimes. *Phys. Fluids* **16** (5), 1449–1466.

DAVIS, P. J. 1979 *Circulant Matrices*. Wiley-Interscience.

FELTEN, F. N. & LUND, T. S. 2006 Kinetic energy conservation issues associated with the collocated mesh scheme for incompressible flow. *J. Comput. Phys.* **215** (2), 465–484.

GRAY, R. M. 2006 Toeplitz and circulant matrices: a review. *Found. Trends Commun. Inform. Theory* **2**, 155–239.

HUNT, J. C. R., WRAY, A. A. & MOIN, P. 1988 Eddies, stream and convergence zones in turbulent flows. *Tech. Rep.* CTR-S88. Center for Turbulent Research.

JANG, Y. I. & LEE, S. J. 2007 Visualization of turbulent flow around a sphere at subcritical Reynolds numbers. *J. Vis.* **10** (4), 359–366.

KIM, H. J. & DURBIN, P. A. 1988 Observations of the frequencies in a sphere wake and of drag increase by acoustic excitation. *Phys. Fluids* **31** (11), 3260–3265.

MITTAL, R. & NAJJAR, F. M. 1999 Vortex dynamics in the sphere wake. *AIAA Paper* 99-3806.

MORINISHI, Y., LUND, T. S., VASILYEV, O. V. & MOIN, P. 1998 Fully conservative higher order finite difference schemes for incompressible flow. *J. Comput. Phys.* **143** (1), 90–124.

Norberg, C. 1998 LDV-measurements in the near wake of a circular cylinder. In *Advances in Understanding of Bluff Body Wakes and Vortex-Induced Vibration: Proceedings of the 1998 Conference*, Washington, DC.

Ploumhans, P., Winckelmans, G. S., Salmon, J. K., Leonard, A. & Warren, M. S. 2002 Vortex methods for a direct numerical simulation of three-dimensional bluff body flows: applications to the sphere at $Re = 300$, 500 and 1000. *J. Comput. Phys.* **178**, 427–463.

Prasad, A. & Williamson, C. H. K. 1997 The instability of the shear layer separating from a bluff body. *J. Fluid Mech.* **333**, 375–402.

Rhie, C. M. & Chow, W. L. 1983 Numerical study of the turbulent flow past an airfoil with trailing edge separation. *AIAA J.* **21**, 1525–1532.

Sakamoto, H. & Haniu, H. 1990 A study on vortex shedding from spheres in a uniform flow. *J. Fluids Engng* **112**, 386–392.

Schlichting, H. 1979 *Boundary Layer Theory*, 7th edn. McGraw-Hill

Seidl, V., Muzaferija, S. & Peric, M. 1998 Parallel DNS with local grid refinement. *Appl. Sci. Res.* **59**, 379–394.

Soria, M., Pérez-Segarra, C. D. & Oliva, A. 2002 A direct parallel algorithm for the efficient solution of the pressure-correction equation of incompressible flow problems using loosely coupled computers. *Numer. Heat Transfer* B **41**, 117–138.

Soria, M., Pérez-Segarra, C. D. & Oliva, A. 2003 A direct Schur–Fourier decomposition for the solution of the three-dimensional Poisson equation of incompressible flow using loosely coupled parallel computers. *Numer. Heat Transfer* B **43** (5), 467–488.

Swarztrauber, P. N. 1977 The methods of cyclic reduction, Fourier analysis and the FACR algorithm for the discrete solution of Poisson's equation on a rectangle. *SIAM Rev.* **19**, 490–501.

Taneda, S. 1978 Visual observations of the flow past a sphere at Reynolds numbers between 10^4 and 10^6. *J. Fluids Mech.* **85** (1), 187–192.

Tomboulides, A. & Orszag, S. A. 2000 Numerical investigation of transitional and weak turbulent flow past a sphere. *J. Fluids Mech.* **416**, 45–73.

Tomboulides, A. G., Orszag, S. A. & Karniadakis, G. E. 1993 Direct and large-eddy simulation of axisymmetric wakes. In *31st Aerospace Sciences Meeting and Exhibit, AIAA Paper* 93-0546.

Verstappen, R. W. C. P. & Veldman, A. E. P. 2003 Symmetry-preserving discretization of turbulent flow. *J. Comput. Phys.* **187**, 343–368.

Yun, G., Kim, D. & Choi, H. 2006 Vortical structures behind a sphere at subcritical Reynolds numbers. *Phys. Fluids* **18**.